

Radiative Recombination Processes in Halide Perovskites Observed by Light Emission Voltage Modulated Spectroscopy

Rafael S. Sánchez,* Alexis Villanueva-Antolí, Agustín Bou, Marta Ruiz-Murillo, Iván Mora-Seró, and Juan Bisquert*

The kinetics of light emission in halide perovskite light-emitting diodes (LEDs) and solar cells is composed of a radiative recombination of voltage-injected carriers mediated by additional steps such as carrier trapping, redistribution of injected carriers, and photon recycling that affect the observed luminescence decays. These processes are investigated in high-performance halide perovskite LEDs, with external quantum efficiency (EQE) and luminance values higher than 20% and 80 000 Cd m⁻², by measuring the frequency-resolved emitted light with respect to modulated voltage through a new methodology termed light emission voltage modulated spectroscopy (LEVS). The spectra are shown to provide detailed information on at least three different characteristic times. Essentially, new information is obtained with respect to the electrical method of impedance spectroscopy (IS), and overall, LEVS shows promise to capture internal kinetics that are difficult to be discerned by other techniques.

1. Introduction

Halide perovskites are very effective photovoltaic materials with high radiative quantum yields^[1–5] that can be applied to excellent performance light-emitting diodes (LEDs).^[6–9] Recently, the fabrication of superior-quality solar cell devices has enabled a detailed analysis of recombination and light emission phenomena.^[10–12] Physically, radiative recombination consists of a band-to-band recombination event connected to light absorption by reciprocity relations.^[13,14] However, the observed recombination rates can be affected by a number of additional effects, which make the photoluminescence (PL) and electroluminescence (EL) kinetics of perovskite nanocrystals longer than the radiative lifetime.^[15] Different electronic/photonic phenomena have been discussed in the literature: carrier trapping,^[16–18] redistribution of injected carriers,^[19–21] photon recycling,^[22–24]

and discharge of the carriers at the contact layers;^[12,25–27] however, these phenomena are currently not very well understood.

The light emission kinetics in perovskite LEDs and in organic light-emitting diodes (OLEDs) is usually investigated using a range of steady-state and time-resolved methods.^[26,28] Remarkably, frequency-resolved methods such as impedance spectroscopy (IS) are highly effective for the separation of concomitant kinetic phenomena.^[29] The connection between time transients and light-stimulated frequency methods in halide perovskite has been reviewed recently.^[30]

Here, we explore a new experimental measuring technique that can provide significant information about recombina-

tion in high-performance solar cells and LEDs. We analyze the frequency-resolved light emission with respect to an applied modulated voltage, that we denote light emission voltage modulated spectroscopy (LEVS). The main point of this investigation is to reveal significant features of the radiative charge recombination that are difficult to be discerned in other measurement techniques.^[30] This methodology will be especially useful when the radiative recombination event is convoluted with previous electronic carrier steps such as transport, trapping, or contact polarization effects, and/or ionic-related phenomena. It has previously been remarked that the capacitance and luminance of LEDs show correlated features^[21,31,32] and some studies of electrically stimulated light emission spectroscopy have been reported,^[33–35] but unfortunately, a general methodology has not been fully developed.


Here we describe the first LEVS experiments in halide perovskite LEDs and establish an equivalent circuit model to understand the observed spectra, based on the previous experience in IS. We show that the method provides unique information on the recombination processes that cannot be accessed by purely electrical techniques, thus highlighting the interest of this new experimental technique for the characterization of optoelectronic devices, especially those presenting multiple physical phenomena, as it is the case of halide perovskite-based systems.

2. The Transfer Functions of Frequency Resolved Measurements

IS is a general-purpose characterization technique that is used in a large variety of fields to extract dynamic information on any

R. S. Sánchez, A. Villanueva-Antolí, A. Bou, I. Mora-Seró, J. Bisquert
Institute of Advanced Materials (INAM)
Universitat Jaume I
Castelló 12006, Spain
E-mail: rasanche@uji.es; bisquert@uji.es

M. Ruiz-Murillo
IoTens
Castelló 12003, Spain

 The ORCID identification number(s) for the author(s) of this article can be found under <https://doi.org/10.1002/adma.202207993>.

© 2023 The Authors. Advanced Materials published by Wiley-VCH GmbH. This is an open access article under the terms of the Creative Commons Attribution License, which permits use, distribution and reproduction in any medium, provided the original work is properly cited.

DOI: 10.1002/adma.202207993

type of system that is operated electrically.^[36–38] The impedance function $Z = \hat{V} / \hat{I}$ is the transfer function of a sinusoidal voltage \hat{V} with respect to a sinusoidal current \hat{I} at a certain modulation angular frequency ω .^[39] The tilde \hat{x} indicates a small amplitude perturbation quantity with frequency ω superposed to a DC signal. The impedance measurement provides detailed information on the dynamic phenomena at a fixed stationary point of the system. Several stationary bias values are applied successively in order to put the device in the appropriate operating conditions where the linearized model parameters can be extracted. The variation of voltage along different values of the current-voltage curve, and the sweep of frequencies at each voltage point over many decades of frequency, provide extensive experimental information, as physical processes that occur at different time scales can be decoupled. An important tool to deal with such complexity is the rationalization of the data in terms of equivalent circuit models. The circuit enables a representation of the physical connections of the fundamental processes and a suitable interpretation of resistances, capacitors and inductors can be obtained in terms of conduction, polarization, charge transfer, and recombination. IS has been extensively applied to halide perovskites in the last decade and the matter has been extensively reviewed.^[29,40] The distinct types of capacitance present in halide perovskites have been well understood^[41] and they will be used below to build the equivalent circuit models.

Other small perturbation frequency modulated techniques that measure an electrical quantity in response to light stimulation have been extensively used in semiconductor photo-electrochemistry and photovoltaics since 1980s.^[42–46] The classical frequency-resolved methods that use a sinusoidal photon flux $\hat{\Phi}_{in}$ impinging on the sample, are intensity-modulated photocurrent spectroscopy (IMPS), and the intensity-modulated photovoltage spectroscopy (IMVS). IMPS is described by the transfer function of current to light flux,^[47–50] $Q = \hat{I} / q\hat{\Phi}_{in}$. Here q is the elementary charge so that the incoming light flux (Φ_{in} in Ns^{-1} , where N is a number of photons), is expressed as an electrical current $q\hat{\Phi}_{in}$. Similarly, IMVS, for voltage-to-light flux, has a transfer function $W = -\hat{V} / q\hat{\Phi}_{in}$.^[51,52]

The transfer functions of the different frequency techniques are not independent, since they arise from the same underlying mechanisms. As shown by Bertolucci et al.,^[53] they are related by the following form that expresses the small perturbation of the system:

$$\hat{I} = \frac{1}{Z} \hat{V} + Qq\hat{\Phi}_{in} \quad (1)$$

The constraint (1) imposes the following relation:

$$W = QZ \quad (2)$$

These functions and their connections have been developed in recent works in the field of halide perovskites.^[54–57]

While Equation (1) considers three central variables for solar cells characterization, (\hat{I} , \hat{V} , $\hat{\Phi}_{in}$), the analysis of light-emitting systems requires an additional physical parameter, the outgoing light flux $\hat{\Phi}_{out}$. In the new method we present here, the photogenerated light is brought into the picture as a dominant

element for the understanding of light-emitting devices' operation. Hence, we extend Equation (1) as:

$$\hat{I} = \frac{1}{Z} \hat{V} + Qq\hat{\Phi}_{in} - \frac{1}{P} q\hat{\Phi}_{out} \quad (3)$$

In Equation (3) we have introduced the transfer function P for light emission current-modulated spectroscopy:

$$P = \frac{q\hat{\Phi}_{out}}{\hat{I}} \quad (4)$$

We are interested in the transfer function S for light emission voltage-modulated spectroscopy:

$$S = \frac{q\hat{\Phi}_{out}}{\hat{V}} \quad (5)$$

Since the product of $q\hat{\Phi}_{out}$ is an electrical current, S has Ω^{-1} units.

As mentioned above the IMPS and IMVS describe the carrier generation process from the light stimulation. In contrast to this, LEVS probes the light generation process from injected carriers. By definition, LEVS is an inverted IMVS with outgoing instead of incoming light. Recombination and charge generation are complementary processes. However, in light-generating devices, we find a number of carrier transport and dissipation processes coupled with radiative recombination. The understanding of all such processes and their couplings is the goal of the present research. We will use the machinery of equivalent circuit models and their interpretation to deal with the complex LEVS spectra that we observe experimentally.

Different light emission functions hold constraint relations of the style of Equation (2). Previously the light modulation transfer function $M = -\hat{\Phi}_{out} / \hat{\Phi}_{in}$ was introduced and measurements have been reported.^[24,58] We note the relationships that are obtained from (3) by selecting two input/output signals each time:

$$S = \frac{P}{Z} \quad (6)$$

$$M = PQ \quad (7)$$

Hereafter, we ignore the incoming illumination $\hat{\Phi}_{in}$ in order to focus on the analysis of S and Z .

3. Theory of Light Emission Voltage-Modulated Spectroscopy

We now develop a model for the interpretation of the S spectra in LEVS measurements, in combination with IS spectra that can be measured as a complementary information. The model is based on well-understood features that have been amply investigated in the methods of IS,^[29,59] to which we add the equivalent circuit part associated with radiative recombination that is not observed in the electrical impedance measurements.^[30] A list of the elements used is presented in **Table 1**.

Table 1. Equivalent circuit elements and currents.

| | |
|-----------|---|
| C_1 | Contact capacitance |
| C_μ | Chemical capacitance |
| C_g | Geometric bulk capacitance |
| R_s | External series resistance |
| R_1 | Contact charge transfer resistance |
| R_a | Contact inductor resistance |
| R_{nr} | Bulk non-radiative recombination resistance |
| R_{rad} | Bulk radiative recombination resistance |
| L_a | Contact inductor |
| L_d | Radiative delay inductor |
| I_{bc} | The current flowing across the device (not through geometric capacitance) |
| i_{rad} | The current flowing through the radiative resistance |

We start with a description of the equivalent circuit. As shown in **Figure 1A** the model is composed of a “bulk” impedance Z_b that contains the radiative component Z_{rad} , a “contact” impedance Z_c that dominates the low-frequency part, a geometric capacitance in parallel C_g , and a series resistance R_s . Correspondingly, the voltage in the active layer is divided into the potential u related to the separation of the Fermi levels that produce radiative recombination, and a voltage v associated with the potential drop at interface and radiatively inactive zones.

The structure of the circuit is specified in **Figure 1B** and the calculation of impedances is described in detail in the Supporting Information (Appendix A). The contact impedance contains a surface capacitance C_1 , a resistance R_1 , and a chemical inductor structure^[60] composed of the resistance R_a and inductor L_a .^[59,61] Therefore, the contact impedance is:

$$Z_c = \left(iC_1\omega + \frac{1}{R_1} + \frac{1}{R_a(1+i\omega/\omega_a)} \right)^{-1} \quad (8)$$

where ω_a is the characteristic frequency of the contact chemical inductor. The bulk impedance is:

$$Z_b = \left(C_\mu i\omega + \frac{1}{R_{nr}} + \frac{1}{Z_{rad}} \right)^{-1} \quad (9)$$

and the radiative impedance has the expression:

$$Z_{rad} = R_{rad} (1 + \tau_d i\omega) \quad (10)$$

The full impedance model B is given by the expression:

$$Z_{tot} = R_s + \left(C_g i\omega + \frac{1}{Z_b + Z_c} \right)^{-1} \quad (11)$$

According to the analysis provided in the Supporting Information (Appendix B) the LEVS transfer function is:

$$S = \frac{q\hat{\Phi}_{out}}{\hat{V}_{app}} = \frac{Z_{tot} - R_s}{Z_b + Z_c} \frac{Z_b}{Z_{tot}} \frac{\varphi_{out}}{Z_{rad}} \quad (12)$$

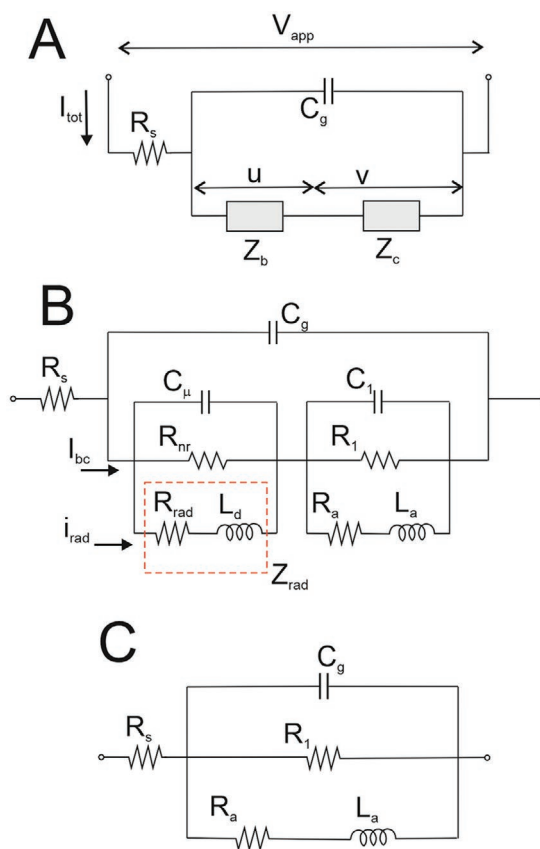


Figure 1. Equivalent circuit models. A) Different parts of the device including a series resistance, R_s , and a geometric capacitance, C_g , in parallel with the bulk, Z_b , and contact, Z_c , impedances, respectively. Voltage acting on C_g is splitted into u and v acting in the bulk and at the contact parts, respectively. B) Similar to circuit A but with Z_b and Z_c detailed. I_{bc} is the total current through the lower branch including radiative and non-radiative processes, see Equation (19), and i_{rad} is the current through the radiative recombination bulk branch, see Equation (26). The part of the circuit corresponding to Z_{rad} , Equation (31), is highlighted with a red dashed rectangle. C) Equivalent circuit used in IS analysis of halide perovskite devices at high applied voltages.

The dc value is:






$$S_0 = \frac{\varphi_{out}}{(R_s + R_b + R_c) \left(1 + \frac{R_{rad}}{R_{nr}} \right)} \quad (13)$$

where φ_{out} is the radiative efficiency, see Appendix B.

Of central importance to this work are the characteristic frequencies shown in **Table 2**. These frequencies can be derived from the equivalent circuit parameters, and they have the important property that the ordering of frequencies in an experimental situation determines different spectral shapes, as discussed in detail in Section 5. This property can be also checked in recent papers for standard light-modulated and impedance techniques.^[54,62]

In our model, we use different RC time constants (ω_h, ω_m) as indicated in Table 2. The contact inductor^[60] frequency ω_a plays an important role in determining the spectral shape. These characteristics are well known from IS methods.^[29]

Table 2. Characteristic frequencies.

| | | |
|-------------------------------------|---|--|
| Contact chemical inductor |  | $\omega_a = \frac{R_a}{L_a}$ |
| Chemical inductor in light emission |  | $\omega_d = \frac{1}{\tau_d}$ |
| Radiative recombination |  | $\omega_\mu = \frac{1}{\tau_{rad}} = \frac{1}{R_{rad}C_\mu}$ |
| RC constant |  | $\omega_h = \frac{1}{R_bC_1}$ |
| RC constant |  | $\omega_m = \frac{1}{(R_b + R_c)C_1}$ |

We also introduce the frequency $\omega_\mu = 1/\tau_{rad}$ that determines the radiative recombination event. In order to describe the experimental data that we have obtained, we consider an additional process contributing to the light emission dynamics. This process represents a preliminary kinetic step with an equilibration time τ_d and frequency $\omega_d = 1/\tau_d$. The physical meaning of such delay is that radiative recombination does not happen until the electron and hole carriers meet at a recombination point. Any carrier transport process that mediates between voltage or light stimulation to the final carrier encounter that results in the emission of a photon, will introduce additional time constants. This picture is very common in the analysis of semiconductor systems requiring a thermalization prior to the recombination of free carrier transport.^[63,64] Different phenomena that affect PL lifetimes of halide perovskites in this way have been identified in the literature: a fast trapping of carriers followed by detrapping, which then leads to radiative recombination,^[15–17] carrier redistribution in response to the applied potential^[19–21,65] and recycling-diffusion events.^[24,66] Our model incorporates the presence of such type of delay by the frequency ω_d .

Equation (13) provides the opportunity to obtain the radiative efficiency of a LED from a quantitative measurement of S_0 , if the different resistances can be separately determined.

4. Experimental Section

LEVS experiments were carried out using halide perovskite LEDs, with CsPbBr₃ nanoparticles as an emitting layer that presents an EL signal centered at 517 nm. The CsPbBr₃ nanoparticles were synthesized according to standard protocols,^[9] with significant variations in the purification procedure to obtain optimum performances; all the methods employed are described in detail in the Supporting Information. Light absorption and PL spectra of colloidal dispersions of CsPbBr₃ nanoparticles are shown in Figure S1, Supporting Information. The LEDs were fabricated using the configuration indicated in Figure 2a:^[67] ITO/PEDOT:PSS/Poly-TPD/CsPbBr₃/POT2T/LiF/Al. The measured LEDs, shown in Figure 2b, were fabricated by subsequent deposition of the corresponding stacked materials by spin-coating (PEDOT:PSS/Poly-TPD/CsPbBr₃) and thermal evaporation (POT2T/LiF/Al). After the fabrication process and encapsulation, four pixels with an active area of 0.08 cm² were available on each 2 × 2 cm ITO substrate.

The device's performance data plotted in Figure S2, Supporting Information, that is, EL spectra and those averaged values of current density, luminance, and external quantum efficiency (EQE), were obtained from more than 20 pixels, thus corroborating a high degree of reproducibility. Note that the studied LEDs display an average luminance and EQE higher than 80 000 Cd m⁻² and 20%, respectively, values that are close to the current records reported for this technology.^[68,69] The LEVS measurements were performed by means of a wavefunction generator, a series of lenses to collimate the emitted light, a fast response photodiode, and an oscilloscope for data acquisition (see Figure S8, Supporting Information, for an illustration of the LEVS setup). Six replicated devices, denoted as LED1 to LED6, were preliminarily characterized to verify the suitability of LEVS. The $q\Phi_{out}$ is measured as a voltage as indicated in Supporting Information and the spectra below were represented in relative scales. Further experimental details about the chemicals

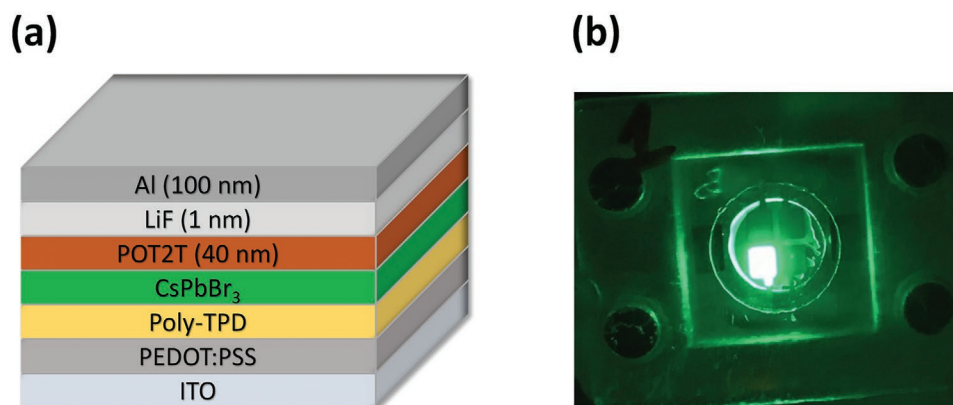


Figure 2. Perovskite LED based on CsPbBr₃ nanocrystals: a) device architecture; b) actual device in operating conditions (4 V) with four active areas of 0.08 cm² each.

and procedures employed for the synthesis and purification of the nanoparticles, LED fabrication, and experimental details of LEVS characterization as well as the equipment utilized for the optical and electro-optical characterization of materials and devices are provided in the Supporting Information.

5. Results

Different experiments have been carried out in order to evaluate the potential of LEVS for perovskite LED characterization. These results will be further discussed in Section 6 using the model detailed in Section 3. The experimental results of the LEVS and IS characterization of the studied CsPbBr₃ LEDs are shown in Figure 3. The real and imaginary parts of transfer functions S and Z are indicated as $S = S' + iS''$; $Z = Z' + iZ''$, respectively. The absolute values of the axis are not relevant, since the outgoing flux has not been measured in absolute terms, see LEVS characterization section in Supporting Information.

The S function of LEVS shows an arc at high frequency. The tendency of the arc is to pass to negative S' at frequencies that lie beyond the experimental window of measurement, see dashed line extrapolation, Figure 3a,b, as confirmed in a separate measurement shown in Figure 4. At low frequency, the spectra enter the fourth quadrant and then return to the first quadrant in a double curling.

The complementary IS measurements are shown in Figure 3c,d, whose spectra display the shape of a high-frequency arc and a chemical inductor feature at low frequency. This shape is very typical of halide perovskite solar cells and memristors at high applied voltage and it has been amply described in recent publications.^[59–61,70] Note that for LEVS characterization, a relatively high voltage (higher than the LED turn-on potential) is needed in order to light the devices up, and therefore, the chemical inductor governs the low-frequency part of the impedance spectra.

While Figure 3a displays well-resolved spectra, those shown in Figure 3b show low resolution due to fast data acquisition. However, the shapes are highly reproducible in different samples, as shown in Figure S3, Supporting Information, and they are voltage-dependent. In some cases, if many points are obtained at a single voltage, then the high-frequency shape is obtained similarly, but in the low-frequency portion, the curling disappears and instead, the S' value decreases monotonically, see Figure 4, or even increases, see Figures 5d and 6b below. This is due to the halide perovskite LED conditioning in continuous operation; see Discussion section for further details. As a general protocol, we bias our halide perovskite LEDs at a constant voltage during a given time (typically few minutes) until the light emission reaches a quasi-steady state, prior to LEVS measurements.

The broadly reported low-frequency response observed in halide perovskite devices is usually ascribed to the ionic nature

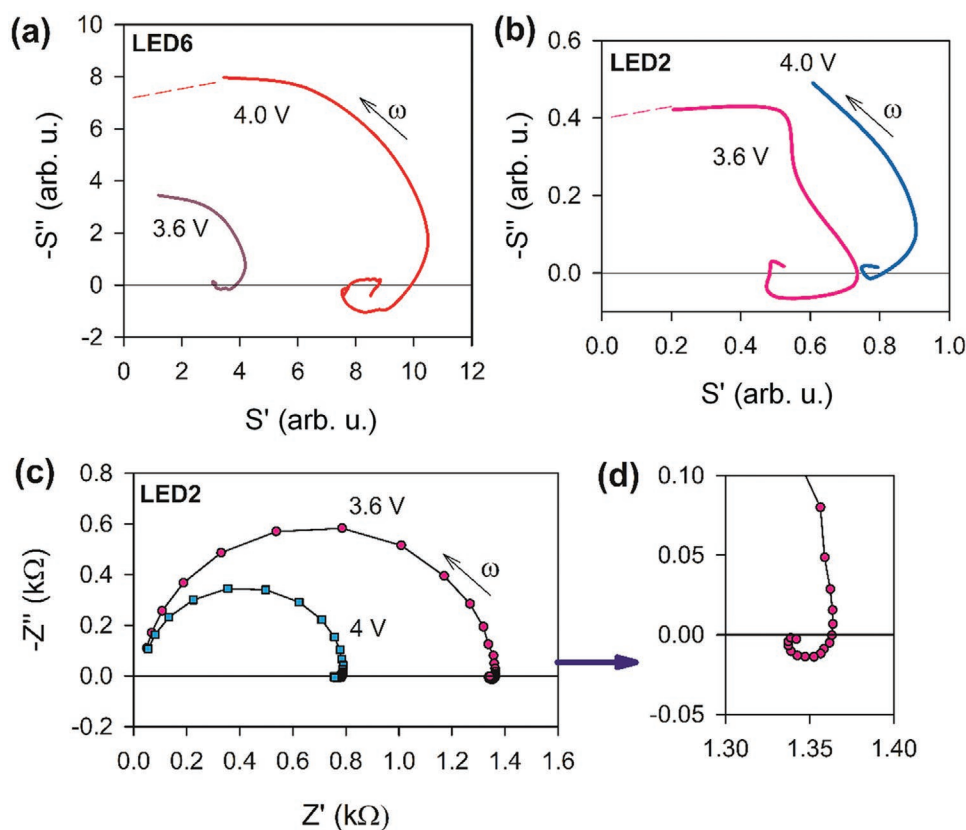


Figure 3. Complex plane representation of: a,b) LEVS of the voltage-driven luminescence transfer function, for different devices at the indicated applied voltages. The dashed lines are a prolongation of the tendency of the data. c,d) Electrical impedance spectra.

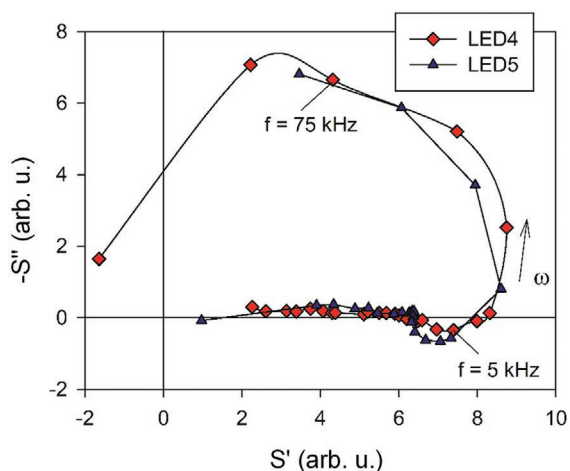


Figure 4. Complex plane representation of the transfer function S of the voltage-modulated EL for two perovskite LEDs at an applied potential of 4 V.

of this family of semiconductors.^[71] The associated ionic migration, which is induced or enhanced upon applying an external electric field and/or under illumination, is believed to promote the generation and/or rearrangement of crystalline defects,^[72] either bulk or interfacial, and therefore, the efficiency of the

devices and their long-term stability are very often seriously compromised. It is worth mentioning that because ion migration is a thermally activated process, the ionic conductivity and related phenomena can be minimized, or even suppressed, by lowering the temperature.^[73]

Aimed at shedding light onto the physical origins of the here observed low-frequency phenomena, the evolution of the EL and voltage of our perovskite-based LEDs was monitored at a constant applied current density at different temperatures (1.65 mA cm^{-2} , that corresponds to an initial luminance (L_0) of $\approx 1000 \text{ Cd m}^{-2}$ at room temperature). As it can be observed in Figure 5a, at sufficiently low temperatures, that is, 223 and 248 K, the EL intensity decreases gradually over time. Contrarily, for higher temperatures, especially obvious at 298 K, an initial EL activation process is detected, and upon few minutes of operation the decrease in the EL intensity is again observed; note that upon 60 min of continuous operation, the EL signals lay at relatively similar levels regardless of the temperature. Simultaneously, the voltage evolution was registered and plotted in Figure 5b; in this case, a gradual voltage drop is consistently observed at the studied temperatures, which indicates that the overall conductivity of the devices is increased over time at any temperature. Note that the voltage at time zero is higher as the temperature is decreased, thus suggesting that the initial conductivity diminishes at lower temperatures. Interestingly,

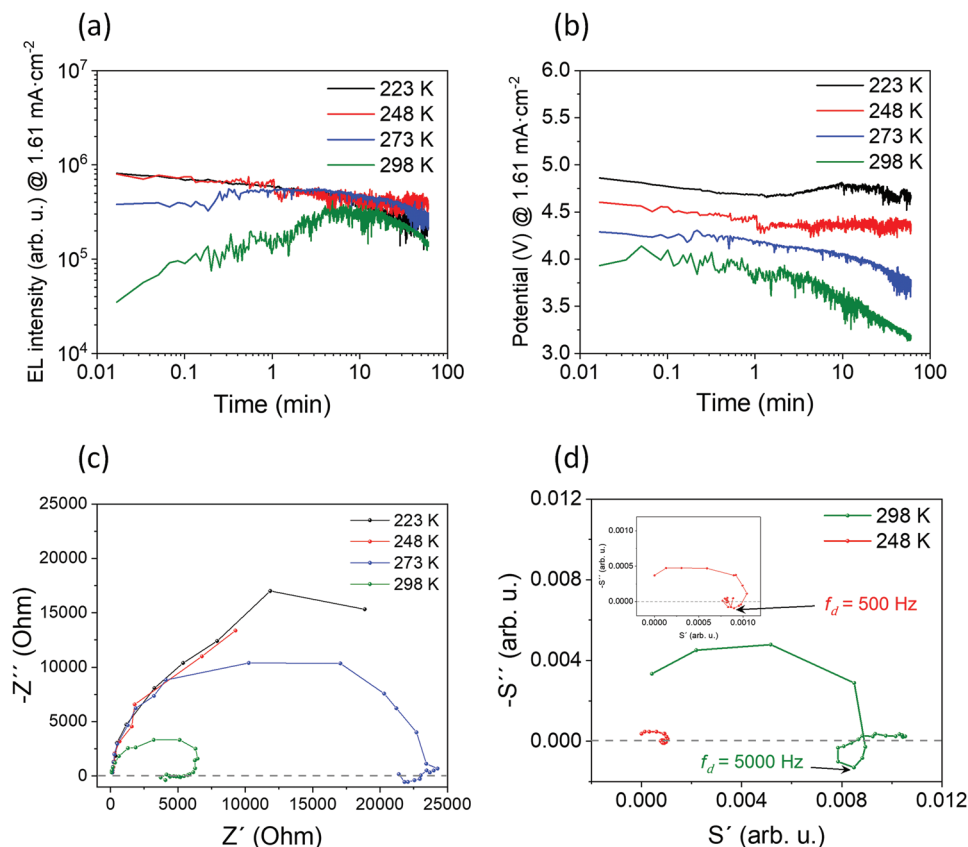


Figure 5. Effect of temperature on the performance of the CsPbBr_3 -based LEDs. a) Evolution of the EL intensity over time at constant current density (1.61 mA cm^{-2}) at different temperatures. b) Evolution of the electrical potential over time (1.61 mA cm^{-2}) at different temperatures. c) Nyquist plots extracted from IS measurements (4 V) at different temperatures. d) LEVS spectra registered at 4 V, both at 298 and 248 K, respectively. Dashed lines indicate the separation between the first and fourth quadrants to highlight the inductive features.

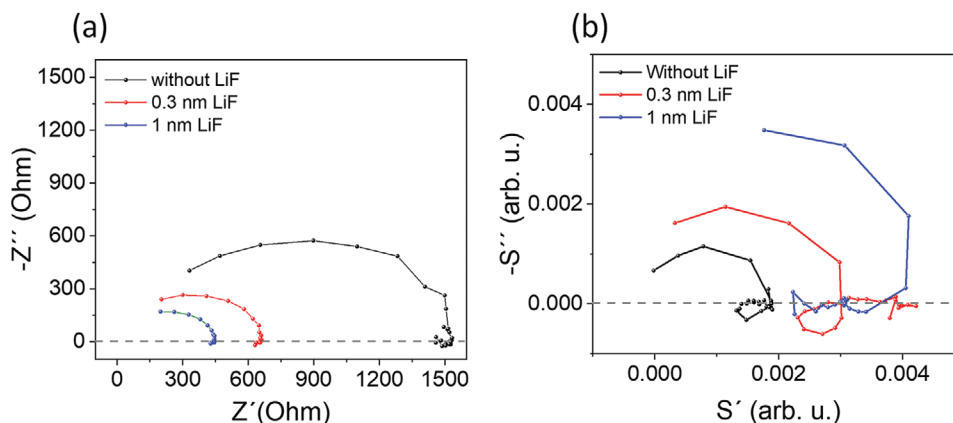


Figure 6. LiF thickness dependence. a) Nyquist plot of the impedance measurements (4 V) at room temperature. b) LEVS spectra (4 V) at room temperature. Dashed lines indicate the separation between the first and fourth quadrants to highlight the inductive features.

the gradual voltage drop occurs at long time-scales (minutes) and it is systematically more noticeable as the temperature is increased, which suggests a direct correlation between the thermally-activated ionic migration, and the slow phenomena observed in perovskite devices, that is, the low-frequency features in IS and LEVS spectra.

It is worth mentioning that the slight voltage increase observed at 223 K, after roughly 2 min of operation (Figure 5b) could be ascribed to an additional electrically-induced phenomenon. We hypothesize that it could correspond to an electrode corrosion mechanism that occurs at the ITO/PEDOT:PSS interface at long timescales (low frequencies) due to the acidic nature of PEDOT:PSS, which was already reported in one of our previous works on LEDs based on II-VI quantum dots.^[74] Nonetheless, the complete elucidation of its origins is beyond the scope of this manuscript.

In order to explore the effect of thermal activation, and therefore look into the contribution of the ionic migration onto the low-frequency response phenomena, according to our reasoning, IS and LEVS spectra at different temperatures were registered. Figure 5c displays the IS spectra acquired between 298 and 223 K and reveals that lower temperatures lead to larger impedance semicircles in the complex plane plots, thus indicating a lower overall electrical conductivity, in agreement with data in Figure 5b. Interestingly, the inductive phenomenon, that is, low-frequency IS signal, becomes only visible at temperatures higher than 273 K, thus suggesting that the low-frequency phenomenon could be directly related to that process that accounts for the EL and voltage evolution witnessed in Figure 5a,b. Unfortunately, the IS spectra at lower temperatures (248 and 223 K) become very noisy in the middle- and low-frequency range due to their huge impedance values (data not shown in the IS spectra at 248 and 223 K), thus impeding the exploration of the region of interest. Contrarily, LEVS measurements allowed us to monitor the behavior of our perovskite LEDs in the full range of frequencies, both, at room and low temperatures, whose spectra are presented in Figure 5d. According to Figure 5a, the EL activation process is suppressed below 248 K, whereas this EL intensity enhancement is clearly detected at room temperature (298 K). Hence, LEVS measurements were only performed at 298 and 248 K,

respectively. As can be clearly observed in Figure 5d, a low-frequency closed loop, that enters the fourth quadrant to then return to the first quadrant, is obtained at room temperature with a characteristic frequency of 5000 Hz (taken at the lowest value of the loop). Even though a loop is also present at 248 K, it remains open and its magnitude is much lower with a tenfold slower characteristic frequency, 500 Hz, thus indicating that this phenomenon is a thermally-activated process, very likely related to the migration of ions as indicated above. Additionally, the magnitude of S' at low temperatures stays almost invariable upon the signal returns to the first quadrant; in contrast, S' increases gradually at room temperature upon looping, contrary to those results obtained for LED4 and LED5 (Figure 4). These apparently inconsistent results at room temperature arise from sample-to-sample variations, most likely due to slightly different conditioning states in which the devices were measured. It is worth reminding that LEVS measures the modulated optical signal, and therefore, considering that the EL of these devices is in continuous evolution upon biasing, as demonstrated in Figure 5a, it is extremely difficult to catch them exactly in the same conditions. Due to the longer acquisition times required at low frequencies, a different evolution of the S' values is manifested.

In this context, our results, which have been obtained through a series of steady-state and modulated techniques, point to ion migration as the main mechanism that accounts for the observed slow dynamics of the perovskite LEDs studied in this work. However, the ion source in this device architecture is not exclusively limited to the perovskite itself, as LiF, which is a compound with strong ionic character, is introduced as an interfacial material. Ultrathin layers of thermally evaporated LiF are usually employed to reduce the work function of metal electrodes^[75] and/or increase the charge mobilities of organic layers,^[76] aimed at enhancing the charge carrier injection in semiconductor devices. Although the beneficial effect of sub-nanometer LiF layers on the performance of devices is broadly documented, the exact mechanisms behind are still controversial and not very well understood.^[77] It is generally accepted that the combination of LiF/Al promotes a suitable electrical contact, through energy-level matching, with a variety of organic materials, thus resulting in ohmic or quasi-ohmic contact.^[78]

In spite of this, some works report on the null effect, or even a detrimental impact on the performance upon introducing a LiF interlayer due to charged defects accumulation.^[79] Aimed at deconvoluting the influence of the perovskite ions and those of the thermally evaporated ionic interfacial layer, a series of LEDs with increasing LiF content were characterized by IS and LEVS, whose results are presented in Figure 6a,b.

Even though decreasing the LiF loading slightly increases the series resistance and gradually, the overall semicircle size, the IS spectra do not show significant qualitative differences in their shapes (Figure 6a); the three samples show the inductive feature at low frequencies, and therefore, the effect of enlarging the interlayer thickness is indeed not very perceptible. Unlike IS data, LEVS spectra displayed in Figure 6b reveal clear differences among samples. First, the samples with lower Z values from IS data (more conductive) show a higher magnitude of S function (more emissive); this is a direct consequence of the larger conductivity of those samples with LiF, which ensure a more efficient charge injection, and therefore, the EL intensity is enhanced. Second, the inductive loop is clearly visible regardless of the LiF content; however, clear differences are evidenced. The control sample, that is, without LiF, displays a closed loop whose S' values remain constant upon looping even at very low frequencies. Contrarily, while S' evolves to the higher values region for that sample with 0.3 nm of LiF, the sample with a thicker interlayer (1 nm LiF) experiences an opposite evolution of the S' function at low frequencies. See Discussion section below for further interpretation details of the overall experimental results.

6. Discussion

We start with the analysis of well-known IS results. As mentioned before, the spectra obtained at high bias voltage show a high-frequency arc and a chemical inductor at low frequency. In the circuit 1C, we have indicated accordingly the information that is actually included in the experimental electrical impedance spectra, while all other elements in the circuit 1B are not resolved. We remark that in many cases the components of the radiative impedance Z_b can be considerably smaller than interfacial-contact recombination, as it is usually observed in high-performance devices.^[30,80] Thus, there is a crucial part of the underlying physical model described by the bulk impedance Z_b that has no significant response in the modulated electrical method of IS. However, this Z_b part of the system is the protagonist for the light emission response and it is captured by the modulated EL transfer function as we discuss in the following.

The spectral shapes of LEVS generated with the model of Equation (12) are shown in Figure 7. We show a series of spectra (a–e) in which the frequency parameter ω_d (red), see Table 2, changes consecutively by one order of magnitude, from 5 to 50 000. In Figure 7a, two separate arcs are obtained and their characteristic frequencies can be clearly assigned. The high-frequency arc corresponds to the radiative inductor $R_{rad}L_d$ with the red frequency $\omega_d = 5$. On the other hand, the low-frequency arc is due to the contact inductor R_aL_a with the brown frequency point ω_a . The RC processes for blue and green frequencies lie at very high frequencies and are not spectrally resolved.

When we increase to $\omega_d = 50$ in Figure 7b, the arc that couples the Z_b resistance and C_1 capacitor, with frequency ω_h (green), see Table 2, becomes manifest at high frequency. The middle arc in Figure 7b corresponds to the light-emission equilibration process associated to ω_d . The low-frequency arc is due to the contact chemical inductor ω_a (brown), which is also clearly present in the impedance spectrum 7f.

In Figure 7c, with a value of $\omega_d = 500$ there is a drastic change in the spectral shape. The spectrum makes a spiral shape, just like our experimental LEVS results shown in the Results section. Each feature is characterized by a separate frequency, from high to low frequencies we obtain distinct arcs due to ω_h , ω_d , and ω_a , respectively. The spectrum shown in Figure 7c will be our reference for the interpretation of the measured spectra. In Figure 7d,e for $\omega_d = 5000$ and 50 000, respectively, the spectra have similar shapes with some features expanded and others reduced. Note that in these cases, S spectra at high frequencies expand clearly into the second quadrant of the complex plane at high frequency, as it is further discussed below. The low-frequency curling features in S are absent in the spectra of a commercial blue LED, shown in Figure S3, Supporting Information, due to much faster response, that is beyond the experimental sensitivity of our current experimental setup, compared to that of the halide perovskite LEDs.

It is remarkable that all the different spectra presented in Figure 7a–e have the same associated impedance spectrum, shown in Figure 7f. In the IS spectra, the high-frequency arc corresponds to ω_m that considers the resistance $R_b + R_c$. The changes of ω_d do not affect the measured electrical impedance Z , since electrically R_{rad} is a minor feature. This fact confirms the unprecedented high sensitivity of LEVS to the processes determining the generation of light.

We have previously introduced the characteristic frequency ω_μ (blue), see Table 2, associated with the radiative recombination event. The radiative lifetime τ_{rad} is estimated in Figure S4, Supporting Information, from the values in the literature. It is expected to have a very low value at high voltage. A very small value of C_μ has been adopted in the simulations of Figure 7, hence ω_μ is the highest value among the characteristic frequencies in the simulation. In Figure 7e, when the value $\omega_d = 50\,000$ becomes comparable to ω_μ , a new feature appears in which the spectrum enters the negative range for the real part S' at the highest frequencies. In Figure 8a the value of the chemical capacitance is increased with respect to Figure 7, and the negative spectral feature is observed. We have remarked that the experimental spectra do show a tendency to pass to negative values at high frequencies. This gives a clear chance to measure τ_{rad} by this method, see Figure S4, Supporting Information. Furthermore, Figure 8b shows that just by changing a factor of 10 the chemical capacitance, there is a flip of two characteristic frequencies and the spectrum folds onto itself changing the shape significantly. These results demonstrate the high sensitivity of the method to the relative values of the characteristic frequencies.

Very interestingly, Figure S6, Supporting Information, shows the high dependence of the spectral shape on the value of the series resistance. With a large R_s value the spectra make a closed loop at the lowest frequency value, which is experimentally corroborated in Figure S7, Supporting Information. Again,

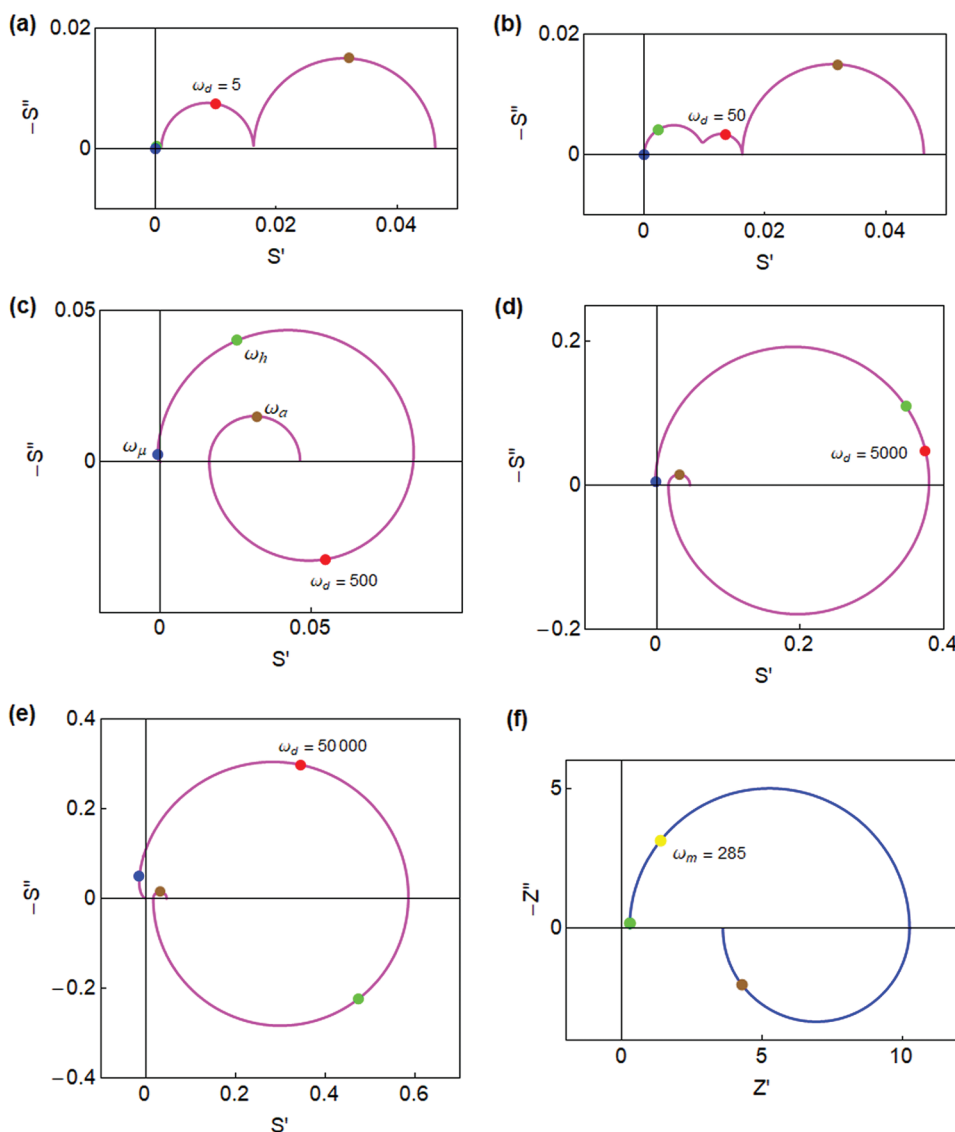


Figure 7. Effect of the light emission frequency ω_d . Representation of a–e) transfer function S of voltage-modulated luminescence and f) impedance Z_{tot} in the complex plane. The parameters are $[R_s, R_{\text{rad}}, R_3, R_1, R_a, C_g, C_1, C_{\mu}, L_a] = [0.1, 1, 0.2, 10, 5, 1.1 \times 10^{-7}, 10^{-3}, 10^{-5}, 5000]$ and $[\omega_{\mu}, \omega_h, \omega_a] = [6 \times 10^5, 6000, 0.001]$, $\varphi_{\text{out}} = 1$. In (a–e) ω_d is varied as indicated. Note that in (f) the value of ω_d is irrelevant for the spectral shape. The circuit elements have dimensionless values to illustrate the shape of spectra. The characteristic frequencies are indicated with the color highlighted in Table 2.

this is a clear new property with respect to IS where the effect of R_s is a simple shift along the real axis.

In studies of photoelectrochemical systems by IMPS, it is a well-established practice to determine characteristic frequency directly from the arc features, instead of model fitting. One typically compares recombination times and charge extraction times by this method.^[42,45,46] Here, we use a similar approach for the analysis of our experimental LEVS spectra. Based on the spectral shape of Figure 7c, the frequencies f_h, f_d, f_a , (related to angular frequencies of the model where $f = \omega/2\pi$), can be obtained by reading the frequency at the top/bottom of each arc. The results are quite reproducible for 6 different replicated devices (Figure S5, Supporting Information). From the IS data, we can only obtain two characteristic frequencies. The frequency of the low-frequency inductor f_a in IS (star points)

matches well the results of LEVS, indicating that the same process has been recorded. The high-frequency arc of S measures f_h that contains the bulk resistance value R_b . Such value cannot be measured in IS that detects the much larger contact resistance and hence the observed arc is related to ω_m . Therefore, it is reasonable that the star points are smaller than the S frequencies for this process. Concerning the frequency f_d that corresponds to the equilibration of recombining carriers, it has a value of about 5000 Hz at room temperature, and it has no correspondence in IS. A device with an added series resistance shows a significant decrease in the characteristic frequencies, Figures S5 and S7, Supporting Information.

To highlight the potential of the new methodology, we have compared LEVS and IS in three different situations. Preliminarily, we have compared the characteristics times obtained

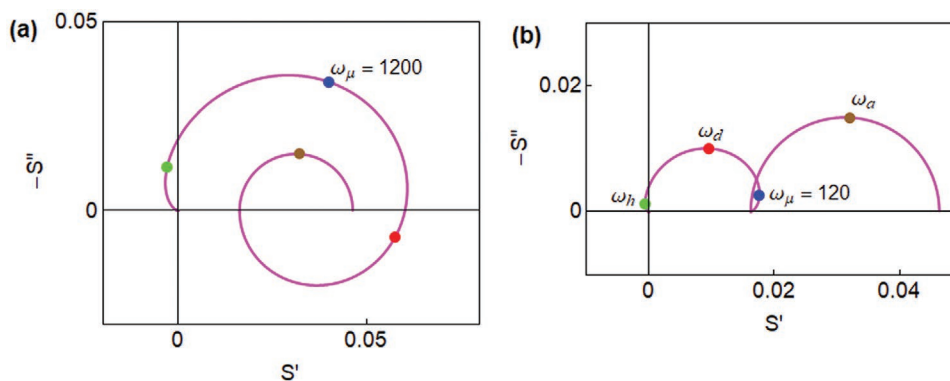


Figure 8. Effect of the chemical capacitance. Representation of transfer function S of voltage-modulated luminescence in the complex plane. The parameters are $[R_s, R_{\text{rad}}, R_3, R_1, R_a, C_g, C_1, L_a] = [0.1, 1, 0.2, 10, 5, 10^{-7}, 10^{-3}, 5000]$ and $[\omega_h, \omega_d, \omega_a] = [6000, 500, 0.001]$, $\varphi_{\text{out}} = 1$. a) $C_\mu = 0.05$, b) $C_\mu = 0.005$. The circuit elements have dimensionless values to illustrate the shape of spectra. The characteristic frequencies are indicated with the color highlighted in Table 2.

with both techniques, see Figure S5, Supporting Information. Then, we have analyzed the effect of temperature that affects drastically the ion migration dynamics, see Figure 5, and finally, we have studied the effect of LiF loading, see Figure 6. In all these cases, it can be clearly concluded that LEVS provides much richer information than IS when it comes to light-emitting devices. Upon careful analysis of the acquired data, we interpret the observed phenomena as follows:

- i) the loop systematically observed in our LEVS measurements must be unambiguously ascribed to ionic migration belonging to the perovskite. Note that the sample without LiF shows a clear closed loop, and upon lowering the temperature, even though it is still visible, its contribution and dynamics, see Figure 5d, are significantly decreased due to a notable restriction of the ionic mobility.
- ii) It has been demonstrated that LiF plays an important role in enhancing the charge injection in OLEDs, as electron mobility is usually much lower than that of the holes for the corresponding organic charge selective contacts.^[81] Nonetheless, it is widely reported that thermally evaporated LiF films show a granular and porous morphology, with large surface roughness.^[82–84] Moreover, due to its effectiveness in the sub-nanometer thickness range, the LiF layers obtained suffer from deficient surface coverage. All these features contribute actively towards the creation of preferential channels through which the charges are more prone to be injected into the electron transport material (ETM); in fact, our fresh samples show tiny dark regions evenly distributed along the light-emitting area under device operation, that correspond to more resistive regions through which the charge carrier conductivity is hampered. Upon applying an external bias, due to their reduced size and their characteristic ion mobilities, Li^+ and/or F^- ions are prone to migrate through organic layers,^[85] the ETM in our case, thus smoothing the granulated structure of the LiF layer and enhancing the overall conductivity of the device over time. This effect can be noticed by naked eye, since throughout the bias conditioning, the dark regions at the device's active area become gradually brighter and the global EL intensity is notably enhanced, see Figure 5a. Upon few minutes,

- the EL intensity starts decreasing, presumably, due to an excessive electrically-induced ionic migration, potentially ascribed not only to perovskite but also to LiF, which could generate a critical density of trap-states, and therefore, new non-radiative charge recombination paths become activated.
- iii) We have found that the LiF loading induces a profound impact on the characteristic times of the EL activation/deactivation processes. Considering the poor control over thickness of such thermally evaporated sub-nanometer thin layers and the continuous evolution of the emission intensity of the devices, it is not surprising that LEVS spectra show clear differences in the aforementioned evolution of the S function, which depend on the conditioning state of the devices and on the slight sample-to-sample variations during fabrication. More precisely, if the evolution of the EL intensity is in the uphill region, S' will shift to higher values at the lowest frequencies; contrarily, if the EL intensity is in the downhill evolution state, the S' will accordingly evolve to lower values. We suggest that all these ionic phenomena contribute to the characteristic inductive behavior of perovskite devices.

In summary, our experimental evidence perfectly match with the predictions thrown by the theoretical model developed here, where two classes of inductors are considered, a chemical inductor ascribed to the perovskite itself (L_d), and a contact chemical inductor (L_a) that we associate to the LiF interlayer. It is worth highlighting that IS characterization does not provide much insight into these effects, as the overall electrical current at constant voltage is in continuous growth regardless of the EL intensity, and therefore, the only phenomenon observed is the gradual reduction of the impedance semicircles upon consecutive IS measurements.

Although we have been unable to measure the radiative lifetime using the LEVS methodology, as it lies beyond our measurement window, further improvement of the experimental setup would allow the experimental determination of ω_{rad} . Nevertheless, we have identified a previous slowing down step that affects the light emission characteristic time. It is worth mentioning that here, there exist different possibilities for the reorganization process, as mentioned earlier: trapping and detrapping, carrier redistribution as a response to the applied

potential, and recycling and diffusion effects. Very importantly, we have succeeded in identifying the origins of the observed phenomena by combining steady-state and modulated techniques, including low-temperature measurements, to deconvolute their impact on the overall functioning of the devices. Our current work is focused on extending the knowledge about the working principles of perovskite LEDs by refining the LEVS methodology and exploiting complementary techniques, such as transient methods in the time domain, to broaden the scope of our research on optoelectronic devices.

7. Conclusions

The characterization of light-emitting devices by frequency-resolved methods offers a great potential for the understanding of those systems in which radiative recombination is combined with a range of carrier transport and contact processes. When the system is stimulated electrically, those processes respond in combination with the light emission event and the interpretation of dynamic measurements becomes rather complex. Here we use a large tradition of disentangling the components of the measured response in the frequency domain using equivalent circuit methods, as it is applied in IS. Very often, the electrical components of the system that are responsible for the radiative light emission, are obscured by other electrical elements in the system. We reasoned that measuring the modulated outgoing light will reveal clearly the kinetic components of the different processes that lead to voltage-stimulated light emission. We developed accordingly a novel experimental technique, that is, LEVS, for the study of halide perovskite LEDs (and other light-emitting devices), including a theoretical physical interpretation and its correlation to a rational understanding of the experimental results, upon measuring a range of high-performance halide perovskite LEDs based on CsPbBr₃ nanoparticles with high reproducibility. We designed a model based on an equivalent circuit that contains the usual features measured in IS plus new elements, that resolve in detail the internal processes that induce the radiative and non-radiative charge recombination. Although the radiative lifetime of the halide perovskite LEDs lies beyond the available measuring frequency range, LEVS has shown an enormous potentiality for the characterization of light-emitting devices. The spectra are characterized by three different characteristic frequencies; two of them can be interpreted in terms of the known characteristic features in the electrical impedance spectra, but a new process indicates a significant reorganization of carriers prior to the radiative event. Our analysis demonstrates that the method shows high sensitivity to the radiative part of the impedance, and provides information on the additional kinetic steps that precede radiative recombination. This technique offers great promise for the characterization of not only high-performance perovskite-based LEDs and solar cells, but also for other opto-electronic devices based on different technologies.

Appendix A: Derivation of the Impedance Function

To develop the model of the electrical impedance, including the recombination model, we use the methods that have been recently

summarized.^[30] We assume a homogeneous distribution of carriers under applied voltage V_{app} and the active layer thickness d . We define the radiative (U_{rad}) and non-radiative (U_{nr}) recombination rates as follows^[11,86]

$$U_{rad} = B_{rad}n^2 \quad (14)$$

$$U_{nr} = \frac{n}{\tau_{nr}} \quad (15)$$

Here n is the carrier density, B_{rad} is the radiative recombination coefficient,^[87] and τ_{nr} is a Shockley–Read–Hall defect-mediated non-radiative recombination lifetime. The radiative recombination lifetime is defined as:

$$\tau_{rad} = \left(\frac{\partial U_{rad}}{\partial n} \right)^{-1} = \frac{1}{2B_{rad}n} \quad (16)$$

Using the intrinsic carrier density n_i we can express the lifetime as a function of the voltage u that is related to the separation of the Fermi levels (Figure 1A)

$$\tau_{rad} = \frac{1}{2B_{rad}n_i} e^{-qu/k_B T} \quad (17)$$

Here k_B is Boltzmann's constant and T the absolute temperature. Normally, the radiative lifetime in Equation (12) is observed at high voltage,^[12,26] while at low voltage the constant non-radiative lifetime dominates, as described by the expression:

$$\tau_{nr} = \left(\frac{\partial U_{nr}}{\partial n} \right)^{-1} \quad (18)$$

The total current in the lower branch of circuit B is:

$$I_{bc} = qd \frac{\partial n}{\partial t} + qd U_{nr} + i_{rad} \quad (19)$$

The first term on the right side of Equation (19) is the volume variation of charge, the second is the non-radiative recombination, and i_{rad} is the variable radiative recombination current (Figure 1B). For the small perturbation measurements at the angular frequency ω , we use the expansion of Equation (19) to first order and the Laplace transformation $d/dt \rightarrow i\omega$ and we obtain:

$$\hat{I}_{bc} = \left(C_\mu i\omega + \frac{1}{\tau_{nr}} C_\mu + \frac{1}{Z_{rad}} \right) \hat{u} \quad (20)$$

Here we have introduced the chemical capacitance:

$$C_\mu = qd \frac{\partial n}{\partial u} \quad (21)$$

and the radiative impedance:

$$Z_{rad} = \frac{\hat{u}}{\hat{i}_{rad}} \quad (22)$$

The part of the equivalent circuit corresponding to Z_{rad} is highlighted in Figure 1B. The non-radiative recombination resistance is:^[30,88]

$$R_{nr} = \left(qd \frac{\partial U_{nr}}{\partial u} \right)^{-1} \quad (23)$$

It satisfies the equation:

$$R_{nr} C_\mu = \tau_{nr} \quad (24)$$

By Equation (20) we obtain the bulk impedance

$$Z_b = \frac{\hat{u}}{\hat{i}_{bc}} = \left(C_\mu i\omega + \frac{1}{R_{nr}} + \frac{1}{Z_{rad}} \right)^{-1} \quad (25)$$

Z_{rad} in Equation (25) must contain the radiative recombination rate. The steady-state radiative recombination current, see circuit B, is:

$$I_{rad} = qd U_{rad} = qdBn^2 \quad (26)$$

and the radiative lifetime can be expressed^[30]

$$R_{rad}C_\mu = \tau_{rad} \quad (27)$$

where

$$R_{rad} = \left(qd \frac{\partial U_{rad}}{\partial u} \right)^{-1} = \frac{1}{C_\mu 2B_{rad}n} \quad (28)$$

The variable recombination current i_{rad} evolves as:

$$\tau_d \frac{di_{rad}}{dt} = I_{rad}(u) - i_{rad} \quad (29)$$

In the small perturbation approach, we obtain:

$$(1 + \tau_d i\omega) \hat{i}_{rad} = \frac{1}{\tau_{rad}} C_\mu \hat{u} \quad (30)$$

Therefore from Equation (22), we arrive at the result:

$$Z_{rad} = R_{rad} (1 + \tau_d i\omega) \quad (31)$$

The full model for the recombination branch is indicated in Figure 1B. The impedance Z_b has three components. The upper one is the chemical capacitance C_μ , which indicates the storage of carriers available for recombination, as in any standard solar cell model.^[89–91] The second is a non-radiative recombination resistance, that is always present to some extent. The lower branch corresponding to Equation (31) is a chemical inductor that affects the recombination process. At very low frequency, the inductive effect vanishes, and the radiative resistance R_{rad} is achieved.

Now the impedance model B is complete, as it is given by the expression:

$$Z_{tot} = R_s + \left(C_g i\omega + \frac{1}{Z_b + Z_c} \right)^{-1} \quad (32)$$

The dc resistance is:

$$R_{tot} = R_s + R_b + R_c \quad (33)$$

where

$$R_b = \left(\frac{1}{R_{nr}} + \frac{1}{R_{rad}} \right)^{-1} \quad (34)$$

$$R_c = \left(\frac{1}{R_1} + \frac{1}{R_a} \right)^{-1} \quad (35)$$

correspond to the total bulk (R_b) and contact (R_c) resistances, respectively.

Appendix B: Derivation of the LEVS Transfer Function

The output photon flux is proportional to the radiative current indicated in Figure 1B, and it is regulated by a factor φ_{out} that is a radiative efficiency:

$$q\hat{\Phi}_{out} = \varphi_{out} \hat{i}_{rad} \quad (36)$$

In terms of the local voltage we have:

$$q\hat{\Phi}_{out} = \frac{\varphi_{out}}{Z_{rad}} \hat{u} \quad (37)$$

To calculate the transfer function, we need to express \hat{u} as a function of \hat{V}_{app} . The total voltage in Figure 1A is

$$\hat{V}_{app} = \hat{i}_{tot} R_s + \hat{u} + \hat{v} \quad (38)$$

We have

$$\hat{v} = \frac{Z_c}{Z_b} \hat{u} \quad (39)$$

Hence

$$\frac{Z_{tot} - R_s}{Z_{tot}} \hat{V}_{app} = \frac{Z_b + Z_c}{Z_b} \hat{u} \quad (40)$$

Finally

$$\hat{u} = \frac{Z_b}{Z_{tot}} \frac{Z_{tot} - R_s}{Z_b + Z_c} \hat{V}_{app} \quad (41)$$

And we obtain

$$S = \frac{q\hat{\Phi}_{out}}{\hat{V}_{app}} = \frac{Z_{tot} - R_s}{Z_b + Z_c} \frac{Z_b}{Z_{tot}} \frac{\varphi_{out}}{Z_{rad}} \quad (42)$$

When the geometric capacitance C_g is very small, we apply the approximation

$$Z_{tot} - R_s \approx Z_b + Z_c \quad (43)$$

The function S takes the form

$$S = \frac{Z_b}{Z_{tot}} \frac{\varphi_{out}}{Z_{rad}} \quad (44)$$

This simplification works well depending on the relative size of the capacitances in the system.

Supporting Information

Supporting Information is available from the Wiley Online Library or from the author.

Acknowledgements

The authors thank the financial support by the Ministerio de Ciencia e Innovación of Spain (MICINN) and Agencia Estatal de Investigación AEI/10.13039/501100011033 by projects PID2019-107348GB-I00 and STABLE PID2019-107314RB-I00, and by the Generalitat Valenciana with Prometeo Q-Solutions project CIPROM/2021/078.

Conflict of Interest

The authors declare no conflict of interest.

Data Availability Statement

The data that support the findings of this study are available from the corresponding author upon reasonable request.

Keywords

halide perovskites, light-emission kinetics, light-emitting diodes, radiative recombination, solar cells

Received: September 1, 2022

Revised: November 1, 2022

Published online: February 5, 2023

- [1] C. M. Sutter-Fella, Y. Li, M. Amani, J. W. Ager, F. M. Toma, E. Yablonovitch, I. D. Sharp, A. Javey, *Nano Lett.* **2016**, *16*, 800.
- [2] H. Huang, A. S. Susha, S. V. Kershaw, T. F. Hung, A. L. Rogach, *Adv. Sci.* **2015**, *2*, 1500194.
- [3] D. W. deQuilettes, S. Koch, S. Burke, R. K. Paranjli, A. J. Shropshire, M. E. Ziffer, D. S. Ginger, *ACS Energy Lett.* **2016**, *1*, 438.
- [4] I. L. Braly, D. W. deQuilettes, L. M. Pazos-Outón, S. Burke, M. E. Ziffer, D. S. Ginger, H. W. Hillhouse, *Nat. Photonics* **2018**, *12*, 355.
- [5] A. F. Gualdrón-Reyes, S. Masi, I. Mora-Seró, *Trends Chem.* **2021**, *3*, 499.
- [6] M. V. Kovalenko, L. Protesescu, M. I. Bodnarchuk, *Science* **2017**, *358*, 745.
- [7] Y.-H. Kim, G.-H. Lee, Y.-T. Kim, C. Wolf, H. J. Yun, W. Kwon, C. G. Park, T. W. Lee, *Nano Energy* **2017**, *38*, 51.
- [8] M. Yuan, L. N. Quan, R. Comin, G. Walters, R. Sabatini, O. Voznyy, S. Hoogland, Y. Zhao, E. M. Beauregard, P. Kanjanaboos, Z. Lu, D. H. Kim, E. H. Sargent, *Nat. Nanotechnol.* **2016**, *11*, 872.
- [9] L. Protesescu, S. Yakunin, M. I. Bodnarchuk, F. Krieg, R. Caputo, C. H. Hendon, R. X. Yang, A. Walsh, M. V. Kovalenko, *Nano Lett.* **2015**, *15*, 3692.
- [10] S. Wheeler, D. Bryant, J. Troughton, T. Kirchartz, T. Watson, J. Nelson, J. R. Durrant, *J. Phys. Chem. C* **2017**, *121*, 13496.
- [11] T. Kirchartz, J. A. Márquez, M. Stollerfoht, T. Unold, *Adv. Energy Mater.* **2020**, *10*, 1904134.
- [12] C. M. Wolff, S. A. Bourelle, L. Q. Phuong, J. Kurpiers, S. Feldmann, P. Caprioglio, J. A. Marquez, J. Wolansky, T. Unold, M. Stollerfoht, S. Shoaee, F. Deschler, *Adv. Energy Mater.* **2021**, *11*, 2101823.
- [13] C. L. Davies, M. R. Filip, J. B. Patel, T. W. Crothers, C. Verdi, A. D. Wright, R. L. Milot, F. Giustino, M. B. Johnston, L. M. Herz, *Nat. Commun.* **2018**, *9*, 293.
- [14] J. Yao, T. Kirchartz, M. S. Vezie, M. A. Faist, W. Gong, Z. He, H. Wu, J. Troughton, T. Watson, D. Bryant, J. Nelson, *Phys. Rev. Appl.* **2015**, *4*, 014020.
- [15] V. S. Chirvony, K. S. Sekerbayev, H. Pashaei Adl, I. Suárez, Y. T. Taurbayev, A. F. Gualdrón-Reyes, I. Mora-Seró, J. P. Martínez-Pastor, *J. Lumin.* **2020**, *221*, 117092.
- [16] M. J. Trimpl, A. D. Wright, K. Schutt, L. R. V. Buizza, Z. Wang, M. B. Johnston, H. J. Snaith, P. Müller-Buschbaum, L. M. Herz, *Adv. Funct. Mater.* **2020**, *30*, 2004312.
- [17] T. Leijtens, G. E. Eperon, A. J. Barker, G. Grancini, W. Zhang, J. M. Ball, A. R. S. Kandada, H. J. Snaith, A. Petrozza, *Energy Environ. Sci.* **2016**, *9*, 3472.
- [18] V. S. Chirvony, S. González-Carrero, I. Suárez, R. E. Galian, M. Sessolo, H. J. Bolink, J. P. Martínez-Pastor, J. Pérez-Prieto, *J. Phys. Chem. C* **2017**, *121*, 13381.
- [19] H. C. F. Martens, H. B. Brom, P. W. M. Blom, *Phys. Rev. B* **1999**, *60*, R8489.
- [20] W. Brütting, S. Berleb, *Phys. Rev. Lett.* **2002**, *89*, 286601.
- [21] L. Zhang, H. Nakanotani, C. Adachi, *Appl. Phys. Lett.* **2013**, *103*, 093301.
- [22] D. W. deQuilettes, K. Frohna, D. Emin, T. Kirchartz, V. Bulovic, D. S. Ginger, S. D. Stranks, *Chem. Rev.* **2019**, *119*, 11007.
- [23] T. W. Crothers, R. L. Milot, J. B. Patel, E. S. Parrott, J. Schlipf, P. Müller-Buschbaum, M. B. Johnston, L. M. Herz, *Nano Lett.* **2017**, *17*, 5782.
- [24] J. Navarro-Arenas, I. Suárez, A. F. Gualdrón-Reyes, I. Mora-Seró, J. Bisquert, J. P. Martínez-Pastor, *Adv. Opt. Mater.* **2021**, *9*, 2100807.
- [25] D. Kiermasch, A. Baumann, M. Fischer, V. Dyakonov, K. Tvingstedt, *Energy Environ. Sci.* **2018**, *11*, 629.
- [26] L. Krückemeier, Z. Liu, B. Krogmeier, U. Rau, T. Kirchartz, *Adv. Energy Mater.* **2021**, *11*, 2102290.
- [27] Z. S. Wang, F. Ebadi, B. Carlsen, W. C. H. Choy, W. Tress, *Small Methods* **2020**, *4*, 2000290.
- [28] S. Sem, S. Jenatsch, K. Stavrou, A. Danos, A. P. Monkman, B. Ruhstaller, *J. Mater. Chem. C* **2022**, *10*, 4878.
- [29] A. Guerrero, J. Bisquert, G. Garcia-Belmonte, *Chem. Rev.* **2021**, *121*, 14430.
- [30] J. Bisquert, *J. Phys. Chem. Lett.* **2022**, *13*, 7320.
- [31] X. Xiao, T. Ye, J. Sun, X. Qu, Z. Ren, D. Wu, S. Ding, X. W. Sun, W. C. H. Choy, K. Wang, *Appl. Phys. Lett.* **2022**, *120*, 243501.
- [32] S. Chen, W. Cao, T. Liu, S.-W. Tsang, Y. Yang, X. Yan, L. Qian, *Nat. Commun.* **2019**, *10*, 765.
- [33] >R. Chouffot, S. Ibrahim, R. Brüggemann, A. S. Gudovskikh, J. P. Kleider, M. Scherff, W. R. Fahrner, P. R. i. Cabarrocas, D. Eon, P. J. Ribeyron, *J. Non-Cryst. Solids* **2008**, *354*, 2416.
- [34] R. Chouffot, A. Brezard-Oudot, J. P. Kleider, R. Brüggemann, M. Labruere, P. Roca i Cabarrocas, P. J. Ribeyron, *Mater. Sci. Eng., B* **2009**, *159–160*, 186.
- [35] S. Khatavkar, M. Kulasekaran, C. V. Kannan, V. Kumar, P. Nair, B. M. Arora, *2013 IEEE 39th Photovoltaic Specialists Conference (PVSC)*, IEEE, Piscataway, NJ, USA **2013**, pp. 0631–0634.
- [36] A. Lasia, *Electrochemical Impedance Spectroscopy and its Applications*, Springer, New York **2014**.
- [37] V. Vivier, M. E. Orazem, *Chem. Rev.* **2022**, *122*, 11131.
- [38] M. E. Orazem, B. Tribollet *Electrochemical Impedance Spectroscopy, Second Edition*, Wiley, Hoboken, NJ, USA **2017**.
- [39] I. Mora-Seró, G. Garcia-Belmonte, P. P. Boix, M. A. Vázquez, J. Bisquert, *Energy Environ. Sci.* **2009**, *2*, 678.
- [40] E. von Hauff, D. Klotz, *J. Mater. Chem. C* **2022**, *10*, 742.
- [41] M. Taukeer Khan, F. Khan, A. Al-Ahmed, S. Ahmad, F. Al-Sulaiman, *Chem. Rec.* **2022**, *22*, 202100330.
- [42] L. M. Peter, *Chem. Rev.* **1990**, *90*, 753.
- [43] B. H. Erné, D. Vanmaekelbergh, *Electrochim. Acta* **1993**, *38*, 2559.
- [44] P. E. de Jongh, D. Vanmaekelbergh, *Phys. Rev. Lett.* **1996**, *77*, 3427.
- [45] J. E. Thorne, J.-W. Jang, E. Y. Liu, D. Wang, *Chem. Sci.* **2016**, *7*, 3347.
- [46] H. Cachet, E. M. M. Sutter, *J. Phys. Chem. C* **2015**, *119*, 25548.
- [47] S. Ravishankar, C. Aranda, S. Sanchez, J. Bisquert, M. Saliba, G. Garcia-Belmonte, *J. Phys. Chem. C* **2019**, *123*, 6444.
- [48] A. Pockett, G. E. Eperon, T. Peltola, H. J. Snaith, A. B. Walker, L. M. Peter, P. J. Cameron, *J. Phys. Chem. C* **2015**, *119*, 3456.
- [49] A. Riquelme, F. E. Gálvez, L. Contreras-Bernal, H. Míguez, J. A. Anta, *J. Appl. Phys.* **2020**, *128*, 133103.
- [50] N. Parikh, S. Narayanan, H. Kumari, D. Prochowicz, A. Kalam, S. Satapathi, S. Akin, M. M. Tavakoli, P. Yadav, *Phys. Status Solidi RRL* **2021**, *16*, 2100510.
- [51] G. Schlichthörl, S. Y. Huang, J. Sprague, A. J. Frank, *J. Phys. Chem. B* **1997**, *101*, 8141.
- [52] J.-P. Correa-Baena, W. Tress, K. Domanski, E. H. Anaraki, S.-H. Turren-Cruz, B. Roose, P. P. Boix, M. Grätzel, M. Saliba, A. Abate, *Energy Environ. Sci.* **2017**, *10*, 1207.
- [53] L. Bertoluzzi, J. Bisquert, *J. Phys. Chem. Lett.* **2017**, *8*, 172.
- [54] J. Bisquert, M. Janssen, *J. Phys. Chem. Lett.* **2021**, *12*, 7964.

- [55] A. O. Alvarez, S. Ravishankar, F. Fabregat-Santiago, *Small Methods* **2021**, *5*, 2100661.
- [56] A. Bou, A. Pockett, D. Raptis, T. Watson, M. J. Carnie, J. Bisquert, *J. Phys. Chem. Lett.* **2020**, *11*, 8654.
- [57] A. Bou, A. Pockett, H. Cruanyes, D. Raptis, T. Watson, M. J. Carnie, J. Bisquert, *APL Mater.* **2022**, *10*, 051104.
- [58] M. Ansari-Rad, J. Bisquert, *J. Phys. Chem. Lett.* **2017**, *8*, 3673.
- [59] C. Gonzales, A. Guerrero, J. Bisquert, *J. Phys. Chem. C* **2022**, *126*, 13560.
- [60] J. Bisquert, A. Guerrero, *J. Am. Chem. Soc.* **2022**, *144*, 5996.
- [61] E. Hernández-Balaguera, J. Bisquert, *ACS Energy Lett.* **2022**, *7*, 2602.
- [62] J. Bisquert, *Appl. Phys. Rev.* **2022**, *9*, 011318.
- [63] J. Orenstein, M. Kastner, *Phys. Rev. Lett.* **1981**, *46*, 1421.
- [64] T. Tiedje, A. Rose, *Solid State Commun.* **1981**, *37*, 49.
- [65] D. Hong, J. Li, S. Wan, I. G. Scheblykin, Y. Tian, *J. Phys. Chem. C* **2019**, *123*, 12521.
- [66] M. Ansari-Rad, J. Bisquert, *Phys. Rev. Appl.* **2018**, *10*, 034062.
- [67] K. M. M. Salim, E. Hassanabadi, S. Masi, A. F. Gualdrón-Reyes, M. Franckevicius, A. Devižis, V. Gulbinas, A. Fakharuddin, *ACS Appl. Electron. Mater.* **2020**, *2*, 2525.
- [68] A. Fakharuddin, M. K. Gangishetty, M. Abdi-Jalebi, S.-H. Chin, A. R. bin Mohd Yusoff, D. N. Congreve, W. Tress, F. Deschler, M. Vasilopoulou, H. J. Bolink, *Nat. Electron.* **2022**, *5*, 203.
- [69] H. Cheng, Y. Feng, Y. Fu, Y. Zheng, Y. Shao, Y. Bai, *J. Mater. Chem. C* **2022**, *10*, 13590.
- [70] L. Munoz-Diaz, A. J. Rosa, A. Bou, R. S. Sanchez, B. Romero, R. A. John, M. V. Kovalenko, A. Guerrero, J. Bisquert, *Front. Energy Res.* **2022**, *10*, 914115.
- [71] H. Zai, Y. Ma, Q. Chen, H. Zhou, *J. Energy Chem.* **2021**, *63*, 528.
- [72] N. Li, Y. Jia, Y. Guo, N. Zhao, *Adv. Mater.* **2022**, *34*, 2108102.
- [73] R. T. Ginting, E.-S. Jung, M.-K. Jeon, W.-Y. Jin, M. Song, J.-W. Kang, *Nano Energy* **2016**, *27*, 569.
- [74] B. C. Hames, I. Mora-Seró, R. S. Sánchez, *Nano Res.* **2018**, *11*, 1575.
- [75] R. Schlaf, B. A. Parkinson, P. A. Lee, K. W. Nebesny, G. Jabbour, B. Kippelen, N. Peyghambarian, N. R. Armstrong, *J. Appl. Phys.* **1998**, *84*, 6729.
- [76] J. Kido, T. Matsumoto, *Appl. Phys. Lett.* **1998**, *73*, 2866.
- [77] A. Turak, in *Electronic Materials*, Vol. 2, MDPI, Basel, Switzerland, **2021**, pp. 198–221.
- [78] B. F. Bory, P. R. F. Rocha, R. A. J. Janssen, H. L. Gomes, D. M. De Leeuw, S. C. J. Meskers, *Appl. Phys. Lett.* **2014**, *105*, 123302.
- [79] P. R. F. Rocha, H. L. Gomes, K. Asadi, I. Katsouras, B. Bory, F. Verbakel, P. van de Weijer, D. M. de Leeuw, S. C. J. Meskers, *Org. Electron.* **2015**, *20*, 89.
- [80] S.-M. Yoo, S. J. Yoon, J. A. Anta, H. J. Lee, P. P. Boix, I. Mora-Seró, *Joule* **2019**, *3*, 2535.
- [81] J.-H. Jou, Y.-T. Lin, Y.-T. Su, W.-C. Song, S. Kumar, D. K. Dubey, J.-J. Shyue, H.-Y. Chang, Y.-W. You, T.-W. Liang, *Org. Electron.* **2019**, *67*, 222.
- [82] F. Cosset, A. Celerier, B. Barelaud, J.-C. Vareille, *Thin Solid Films* **1997**, *303*, 191.
- [83] F. Gołek, P. Mazur, *Surf. Sci.* **2003**, *541*, 173.
- [84] S. I. Lee, K. Liang, L. S. Hui, R. Arbi, M. Munir, S. J. Lee, J. W. Kim, K. J. Kim, W. Y. Kim, A. Turak, *J. Mater. Sci.: Mater. Electron.* **2021**, *32*, 1161.
- [85] C.-I. Zhang, F.-c. Wang, Y. Zhang, H.-x. Li, S. Liu, *Int. J. Photoenergy* **2010**, *2010*, 291931.
- [86] F. Staub, H. Hempel, J.-C. Hebig, J. Mock, U. W. Paetzold, U. Rau, T. Unold, T. Kirchartz, *Phys. Rev. Appl.* **2016**, *6*, 044017.
- [87] C. Barugkin, J. Cong, T. Duong, S. Rahman, H. T. Nguyen, D. Macdonald, T. P. White, K. R. Catchpole, *J. Phys. Chem. Lett.* **2015**, *6*, 767.
- [88] J. Bisquert, F. Fabregat-Santiago, I. Mora-Seró, G. Garcia-Belmonte, S. Giménez, *J. Phys. Chem. C* **2009**, *113*, 17278.
- [89] J. Bisquert, *Phys. Chem. Chem. Phys.* **2003**, *5*, 5360.
- [90] I. Mora-Seró, J. Bisquert, F. Fabregat-Santiago, G. Garcia-Belmonte, G. Zoppi, K. Durose, Y. Y. Proskuryakov, I. Oja, A. Belaidi, T. Dittrich, R. Tena-Zaera, A. Katty, C. Lévy-Clement, V. Barrioz, S. J. C. Irvine, *Nano Lett.* **2006**, *6*, 640.
- [91] J. Bisquert, *The Physics of Solar Energy Conversion*, CRC Press, Boca Raton, FL, USA **2020**.